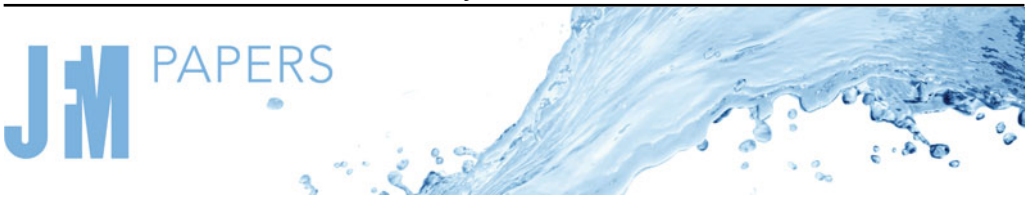
J. Fluid Mech. (2025), *vol.* 1021, A15, doi:10.1017/jfm.2025.10633



Microscopic salt exclusion dynamics of directional freezing in brine

Zhaohao Wu[1,2], **Xiangbo Gao**[1,2], **Jinbo Jia**[2], **Yingbo Jiang**[1,2], **Herbert E. Huppert**[3] **and Liang Lei**[2,4,5]

[1]College of Environmental and Resource Sciences, Zhejiang University, Hangzhou, Zhejiang, 310058, PR China

[2]School of Engineering, Westlake University, Hangzhou, Zhejiang, 310030, PR China

[3]Institute of Theoretical Geophysics, King's College, University of Cambridge, King's Parade, Cambridge, CB2 1ST, UK

[4]Research Center for Industries of the Future, Westlake University, Hangzhou, Zhejiang, 310030, PR China

[5]Institute of Advanced Technology, Westlake Institute for Advanced Study, Hangzhou, Zhejiang, 310024, PR China

Corresponding authors: Liang Lei, leiliang@westlake.edu.cn; Xiangbo Gao, gaoxiangbo@westlake.edu.cn

(Received 4 May 2025; revised 16 July 2025; accepted 22 August 2025)

Directional freezing of brine is widely found in numerous environmental and industrial settings. Despite extensive studies, the microscopic evolution of ice-brine structures remains unclear. By combining *in situ* micro-computed tomography visualisation and theoretical analyses, we reveal new details inside the porous ice structure and its evolution towards a cleaner ice layer. We identify three distinct stages characterised by different brine exclusion rates during solidification: a rapid initial stage possibly lasting seconds from nucleation to local equilibrium without long-range heat or mass transfer; a second stage where the system reaches global thermal equilibrium, involving brine expulsion by volume expansion and convection associated with gravity; and a final prolonged stage dominated by diffusion. Comparison between analytical solutions and the migration rates of microstructural features such as brine stripes, columns and pockets extracted from photographic images confirms these understandings. Morphologically, we capture the formation of random striped patterns together with brine columns during downward freezing and brine skirts during upward freezing, all of which gradually transform into vertically aligned polygonal patterns. The volume fraction of brine pockets in porous ice near the cold end reduces to less than 10 % after 22 h in most experiments. The residual brine pockets, however, are not rejected out of the porous ice as fast as predicted by

https://doi.org/10.1017/jfm.2025.10633 Published online by Cambridge University Press

© The Author(s), 2025. Published by Cambridge University Press.

diffusion and remain persistent. Our findings provide new insights into the brine freezing dynamics, with implications ranging from sea ice formation to freeze desalination and general solidification of binary melts.

Key words: sea ice, icing, morphological instability

1. Introduction

Ice forms and coexists with the residual brine when brine solutions are cooled below their freezing point. This phenomenon underpins many critical environmental and technological processes, such as sea ice formation, industrial desalination, biological cryo-preservation and food processing (Chayen & Saridakis 2008; Williams *et al.* 2015; Chen *et al.* 2022; Raphael *et al.* 2025).

Studies of brine freezing cover multiple scales mainly focusing on macroscopic, microscopic and molecular-scale processes. At the macroscopic scale (0.1–1 m), previous studies extensively adopted mushy layer theory (Worster 1990; Wells, Hitchen & Parkinson 2019; Anderson, Guba & Wells 2022; Du *et al.* 2023, 2024), describing ice as a porous, two-phase medium composed of pure ice crystals interspersed with interstitial brine (Feltham *et al.* 2006). A significant feature of sea ice is the formation of brine channels, which are widely assumed to serve as primary pathways for brine rejection (Worster and Rees Jones 2015). Diffusion driven by a salt concentration gradient induced by a temperature gradient is thought to be a major mechanism for the rejection of the brine initially trapped within an ice matrix (Whitman 1926; Notz & Worster 2009), while convection is reported to only be possible when the ice layer exceeds a critical thickness (Worster *et al.* 1997). In addition, the volume expansion during the water–ice phase transition helps to squeeze trapped brine out of the porous ice (Galley *et al.* 2015). At the molecular-scale, various studies, almost all molecular dynamics simulations, have investigated ion rejection (Vrbka & Jungwirth 2005), interfacial instabilities (Chu *et al.* 2024) and nanoscale salt expulsion mechanisms (Tsironi *et al.* 2020; Zhao *et al.* 2023), all of which shape the behaviour of the solidification front. Experimentally, Cryo-SEM has been utilised for imaging of brine veins and pockets (Vetráková *et al.* 2019).

At the microscopic scale ($\sim$10 μm), several attempts have been made to reveal the ice-brine microstructures under a frozen state, particularly the distribution of salt inclusions and the formation of brine networks (Oggier & Eicken 2022). Magnetic resonance imaging (Aussillous *et al.* 2006), Hele-Shaw cells (Katz & Worster 2008; Testón-Martínez *et al.* 2024), confocal or Raman microscopy (Marcellini *et al.* 2016; Malley, Chakraborty & Kahan 2018) and schlieren methods (Middleton *et al.* 2016) have been employed to capture the development of brine channels, displaying how convection-driven pathways (brine channels) form within the ice matrix. However, due to technical limitations and the challenges of real-time imaging at high resolution, most studies on the visualisation of mushy layers have focused only on static final-state structures or two-dimensional observations (Maus, Schneebeli & Wiegmann 2021; Zhang *et al.* 2022; Wang *et al.* 2023; Maus *et al.* 2023; Yang *et al.* 2025). Currently, there are no data capturing the detailed temporal evolution of microstructures, leaving gaps in our understanding of how brine migration and ice morphology change over time.

This work investigates the microscopic dynamics of directional brine freezing through *in situ* X-ray micro-computed tomography (micro-CT) via a cylindrical sample holder, bridging a critical gap in understanding ice-brine structure changes with high resolution. We present four-dimensional (three-dimensional + time) visualisations of the complete

https://doi.org/10.1017/jfm.2025.10633 Published online by Cambridge University Press

freezing process, reveal the evolution of ice-brine structures in detail, identify key stages according to the temporal-spatial scale of the underlying physical processes and further elucidate the influence of the complex coupling dynamics in thermal conduction, phase boundary conditions and mass transport on microscopic purification mechanisms. Unique features observed during freezing, such as brine stripes, columns, skirts and pockets, are discussed with an emphasis on their formation and migration mechanisms. Moreover, gravity, as a critical contributor to brine transport and exclusion, has been investigated to isolate the role of convection.

2. Methods

Below we briefly describe the experimental methods in this study. Further details are included in the Supplementary Information (SI).

Experimental set-up. To compare with seawater freezing, molar concentrations are selected to be 0.3, 0.6 and 1.2 M, out of which 0.6 M is close to the equivalent concentration of natural seawater. Potassium iodide (KI) instead of sodium chloride (NaCl) is used for better contrast between the ice and the unfrozen brine (Lei, Seol & Jarvis 2018). Both KI and NaCl depress the freezing point of brine, following slightly different salt-water phase diagrams (figure S2 draws the phase diagrams of KI and NaCl in the same plot). Diffusivities of different ions in brine are of the same order of magnitude ($\sim 1.8 \times 10^{-5}$ and $\sim 1.5 \times 10^{-5}$ cm^2 s^{-1}) (Hoekstra, Osterkamp & Weeks 1965). The relationship between brine density and salt concentration is also different. Potential effects of these differences on brine directional freezing are further discussed in § 4. The experimental configuration for the *in situ* four-dimensional micro-CT study of brine directional freezing is shown in figure S1 (see details in § S1). A degassed solution was slowly injected into the cylindrical sample holder (1×1 cm) to prepare the specimen. We coated the sample holder with thermal insulation to reduce the lateral heat flux. Two thermocouples (T-36-SLE, *T* type) were inserted at the top and bottom of the specimen to monitor temperatures at the interfaces. Before freezing, the temperature was stabilised at 4 °C for at least one hour to achieve a uniform and reproducible starting point. To explore the effect of gravity, we employed both downward (the cold end at the top) and upward (the cold end at the bottom) freezing boundaries. The freezing was initiated by simultaneously lowering the boundary temperatures (see details in § S2) towards the targeted values (0 °C at the warm end and −9 °C at the cold end). Nucleation in the relatively pure solution was difficult, since the brine specimen was prepared with deionised water and degassed before injected into the sample holder. Therefore, the specimen reaches thermal equilibrium with a one-dimensional linear temperature gradient before the nucleation. Nucleation in the 0.3 mol l^{-1} case occurs spontaneously. For specimens with higher initial salt concentrations, nucleation is stimulated by tapping the side of polyether-ether-ketone holder (figure S1) with a thin metal rod. The mechanical disturbance helps overcome the nucleation barrier in the supercooling solution. Once nucleation is triggered, ice crystals rapidly grow and propagate throughout the supercooled region within seconds. Detailed experimental parameters are documented in table S1.

Micro-CT imaging and scanning. Raw tomograms with a voxel size of 13.7 μm were acquired to provide sufficient resolution for tracking microstructural details. The CT scanning strategy was designed in two phases: an initial phase of 10 consecutive scans (approximately three hours) to capture rapid morphological evolution, followed by periodic scans every 3 h for ∼24 h to track slower processes (see more details in § S3).

https://doi.org/10.1017/jfm.2025.10633 Published online by Cambridge University Press

3. Results and discussion

3.1. *General observations*

Microstructural evolution of ice and the complementary brine manifests unique spatio-temporal features during directional freezing. The brine specimen is under supercooling before nucleation, and the initial temperature profile is linear along the vertical direction between the warm and cold ends, which were maintained at constant temperatures throughout the freezing process. When the nucleation barrier was overcome, numerous ice crystals emerged in several seconds. These nascent crystals, shown as dark areas and coexisting with the bright brine, are disordered, as shown in the CT image taken soon after the nucleation (figure 1). The brine trapped in the porous ice gradually gets pushed out of the porous ice afterwards and accumulates at the warm end. Meanwhile, the boundary between porous ice and pure brine, or the freezing front, advances at first, but retreats later. Within the porous ice, the initially disordered pattern is swiped out towards the warm end by vertically striped patterns. Later, a cleaner layer of ice emerges within the porous ice. In addition, brine localises in the centre to form brine columns during downward freezing, but in the periphery to form brine skirts during upward freezing. Overall, the evolution of trapped brine emulates waterfalls in downward freezing and flames in upward freezing (see SI movies 1 and 2, which are time-lapse animations). The final state of upward freezing at $\sim$24 h resembles that of downward freezing except for the centre column, although the evolution path is obviously different.

The horizontal sections (figure 1*b*,*c*,*e* and *f*) reveal complementary structural evolution in addition to vertical features. Several groups of porous ice with striped patterns emerge soon after nucleation. These groups resemble the distribution of single crystals within polycrystals, which has also been reported in previous research (Kamm 2023). Localisation of unfrozen brine is clearer in downward freezing, and later facilitates the formation of brine columns. We speculated that the location of these brine columns could be associated with group boundaries, but careful investigation of raw images does not support this. Although the vertex of the brine columns shows strong correlation with the group boundaries, the rest of the columns can cut through one group of crystals. The brine in the porous ice structure forms a swirl distribution in figures 1(*b*) and 1(*c*) for the 0.6 mol l^{-1} case, while swirls are absent in both the 0.3 and 1.2 mol l^{-1} cases. All striped and localised brine patterns are swiped by polygonal patterns during the afterward evolution. This transformation from striped to polygonal patterns coincides with the vertical alignment observed in the vertical sections.

The observed initial patterning is unlikely to be caused by the applied mechanical disturbance introduced to facilitate the nucleation. For the cases with 0.3 mol l^{-1}, mechanical disturbance was not required to initiate the nucleation, and these patterns still emerge. The brine stripes and disordered ice crystals are not localised near the tapped site but spread throughout the specimen. We speculate that the first nucleation occurs randomly, while the following propagation spreads from the first nucleation sites. The pattern is governed by the complex interaction between heat and mass transfer, ice-brine interface instability, as well as preferential growth direction associated with symmetry broken in crystallisation.

3.2. *Evolution stages determined by spatial-temporal scales*

The overall directional solidification can be categorised into three transitional stages, separated by four critical states (S1–S4), as detailed in figure 2. Initially (S1), a linear temperature profile is established between the imposed cold and warm boundaries prior to nucleation (grey line in figure 2*a*), where the brine concentration is uniform throughout

https://doi.org/10.1017/jfm.2025.10633 Published online by Cambridge University Press

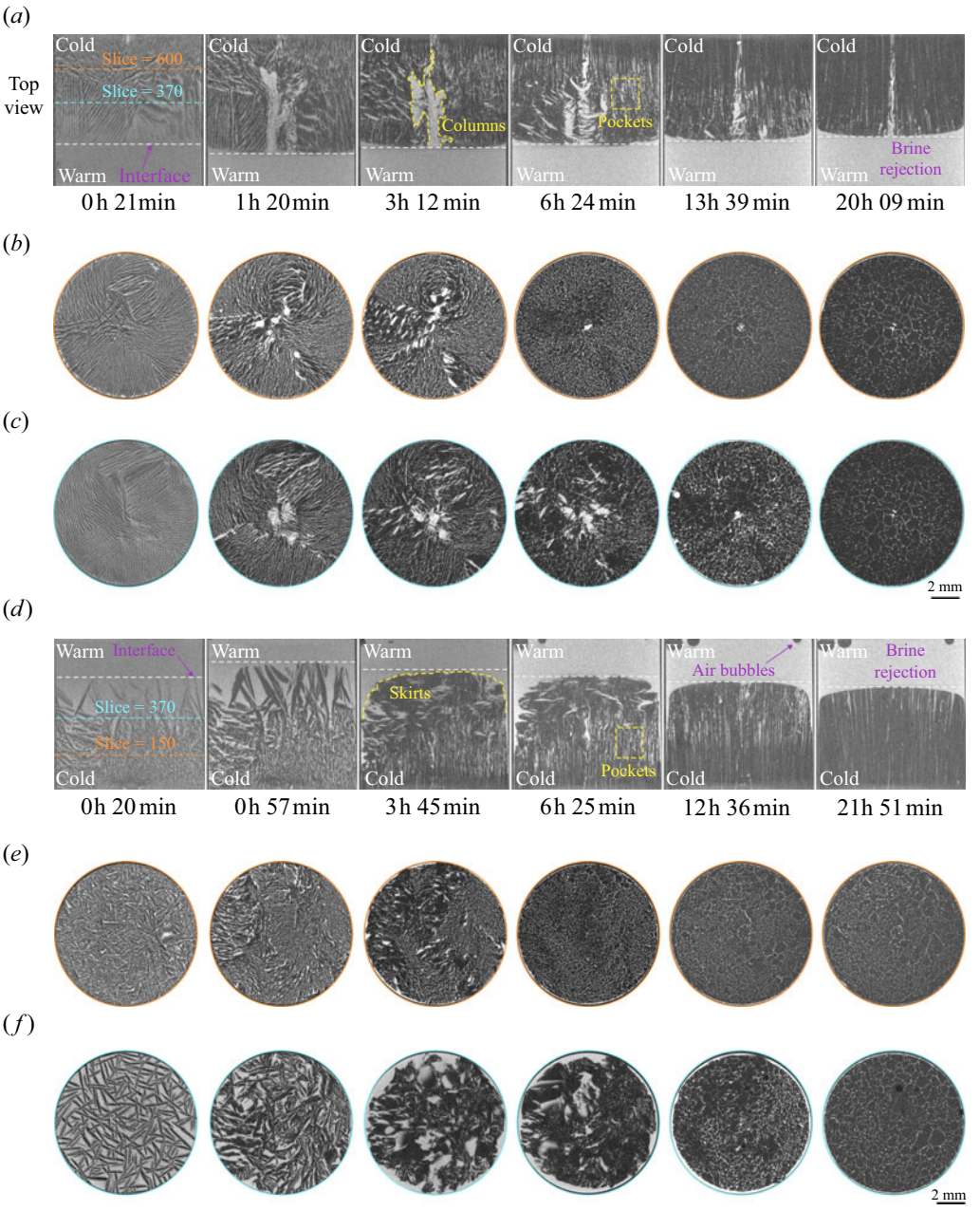


Figure 1. Typical raw images capturing microstructural evolution of brine (bright) and porous ice (dark). Panels (*a*) and (*d*) are time sequences of vertical slice images in downward and upward freezings. Panels (*b*), (*c*), (*e*), and (*f*) are respectively the horizontal slices from bottom to top corresponding to vertical slices at 8.22, 5.07, 5.07 and 2.06 mm out of the 10 mm specimen height. Full time sequences of horizontal and vertical slices are provided in figure S4.

the specimen. Rapid (within seconds) crystal growth occurs after nucleation, and the system then transitions to the S2 state. During this short period, long-range energy and mass transfer can be neglected; and therefore both local energy and mass conservation can be assumed. Latent heat released during this period raises the local temperature (pink

https://doi.org/10.1017/jfm.2025.10633 Published online by Cambridge University Press

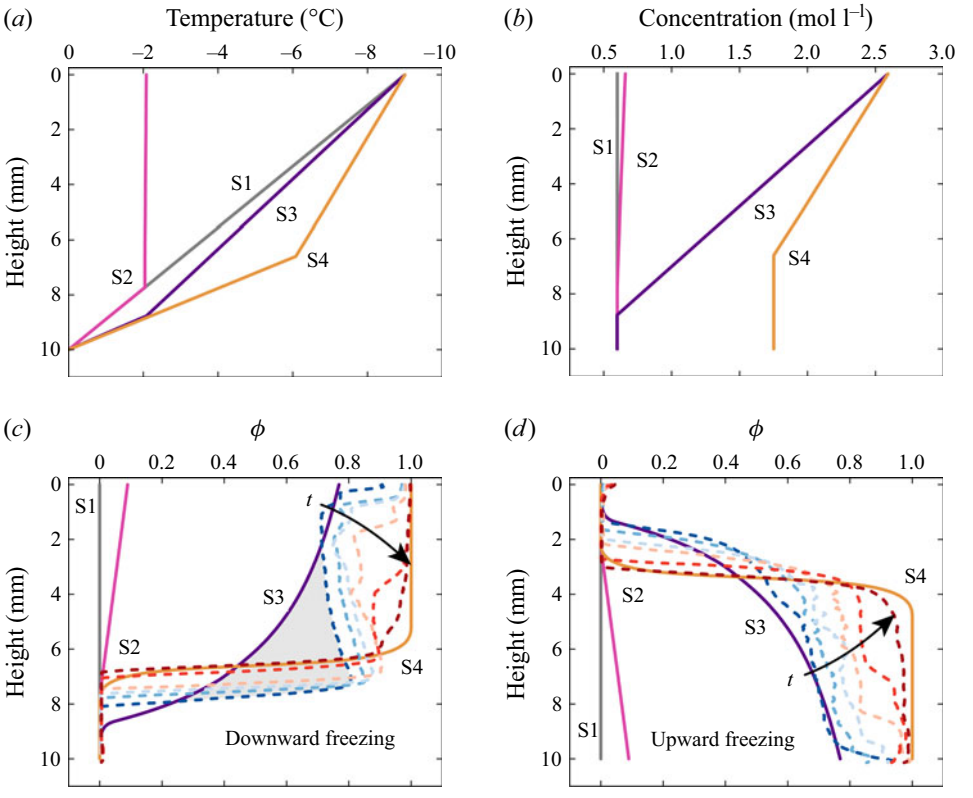


Figure 2. Vertical profiles of (*a*) temperature T, (*b*) concentration C, (*c*) ice volume fraction ϕ of downward freezing and (*d*) upward freezing predicted for four critical states (solid lines) and experimental measurements (broken lines). Note that t indicates freezing duration and, as t increases, the ice volume fraction profiles evolve following the directions of the black arrows.

line). The critical state S3 (purple line) is defined considering that heat transfer is faster than mass migration limited by diffusion, where we consider a steady state of heat transfer is reached while mass migration is yet to take effect. Local mass conservation is still assumed, while one-dimensional heat conduction is used to calculate the local temperature. Since the thermal conductivity of ice is ∼4 times that of water, the range of colder regions enlarges and the freezing front advances. The last transition spanning S3–S4 (yellow line) occurs over a lengthy time compared with earlier stages. Here, brine migration by diffusion plays a dominant role. As ions get purged out of the porous ice, the salt concentration in the pure brine region increases, and the freezing front retreats to a lower temperature as determined by the phase boundary (see the detailed calculation process in § S4).

Figure 2(*c*) illustrates the predictions with solid lines and the volume fraction profiles of ice with broken lines extracted from CT images. The stage from S1 to S2 state (first 20 min) images are omitted because they are blurry, and the process occurs too rapidly for clear visualisation. In general, the broken lines evolve from S3 at one hour (blue broken line) towards S4 at approximately 22 h (red broken line). Note that the actual cases deviate from the ideal predictions because the assumptions are not strictly met. For example, the difference between the blue broken line and purple solid line at $Z = 0$–2 mm is caused by actual mass migration. The ice volume fraction one hour after nucleation (blue broken line) during upward freezing (figure 2*d*) matches well with the predicted value (purple solid line), while the mismatch shown in the grey shadow during downward freezing

https://doi.org/10.1017/jfm.2025.10633 Published online by Cambridge University Press

indicates a quick brine transport mechanism, likely gravity-driven convection, soon after nucleation. Because brine convection accelerates the rejection of condensed brine out of the porous ice, the average salt content within the porous ice decreases, which then allows the formation of more ice at the same temperature. The shorter distribution of ice, only significant in downward freezing, reflects an elevated brine concentration at the ice-brine interface, which is also consistent with the mismatch in the shadow.

Both convection in single brine pockets and larger-scale convection in the porous ice through connected brine pockets is considered. Convection in single brine pockets is possible when the Rayleigh number is larger than 1708 (Wanschura, Kuhlmann & Rath 1996; Shishkina 2021). Meanwhile, between rigid and highly conducting boundaries, convection is verified in inclined systems without a threshold in Rayleigh number (Nield 1994; Daniels, Plapp & Bodenschatz 2000; Ortiz-Pérez & Dávalos-Orozco 2011). However, we should also consider that the thermal expansion coefficient is negative for water when the temperature is below 4 °C, at which the water density reaches a maximum. Considering the temperature within the porous ice layer is mostly below −1 °C, which is below the maximum density temperature even considering the effect of dissolved salt, the direct effect of the temperature gradient should stabilise the fluid. We therefore consider that the density variation due to the salt concentration gradient, which is also associated with the temperature gradient, should be the driving force for convection in the first hour after nucleation. We define an equivalent expansion coefficient β' due to the salt concentration gradient determined by the temperature gradient according to the phase diagram within the porous ice, to obtain a calculated $\beta' \approx 3.28 \times 10^{-2}\ \mathrm{K}^{-1}$, which is two orders of magnitude higher than for pure thermal expansion, for which $\beta \approx -1 \times 10^{-4}\ \mathrm{K}^{-1}$ at −1 °C. This highlights the dominant role of the salt concentration gradient over thermal expansion. Correspondingly, the equivalent Rayleigh number within the 8 mm-thick porous ice, which considers the fluid density change due to both temperature and salt concentration gradients, is approximately 3.2×10^6 (detailed derivation and calculation in § S4). Alternatively, if we enforce the equivalent Rayleigh number to be 1708, then the corresponding critical thickness $L_c = 1.2$ mm, which means that convection is possible in any brine pockets taller than 1.2 mm. Similarly, we can obtain the Darcy–Rayleigh number within the porous ice to evaluate large-scale convection through connected brine pockets. The Darcy–Rayleigh number ranges from 285, when we consider only the fine brine stripes, to 7120, when we look into the thick brine columns. Therefore, convection can only occur within the thick brine columns, in which the analysis with Rayleigh number is more appropriate, but not in porous ice with fine brine stripes. Alternatively, this points to the possibility that the brine columns are the main contributor to the convection. It has been reported that there is a critical thickness, typically several centimetres, for the mushy ice layer to produce convection (Wettlaufer, Worster & Huppert 1997). However, several millimetres of mushy layer is shown to yield convection, which can be related to the applied higher temperature gradient. Furthermore, double diffusion due to the different diffusion coefficients of mass and heat can occur. In addition, brine expulsion caused by volume expansion also contributes to brine exclusion, which can potentially explain the mild difference between the blue broken line and the purple solid line at $Z = 3$–8.5 mm, as shown in figure 2(*d*).

3.3. *Brine columns and skirts*

Brine columns emerge at or near the centre of the specimens in all downward freezing cases. (figure 3*a*, also see SI movie 3). Smaller brine stripes are filtered out in the visualisation to highlight the evolution of major brine columns. These brine columns

https://doi.org/10.1017/jfm.2025.10633 Published online by Cambridge University Press

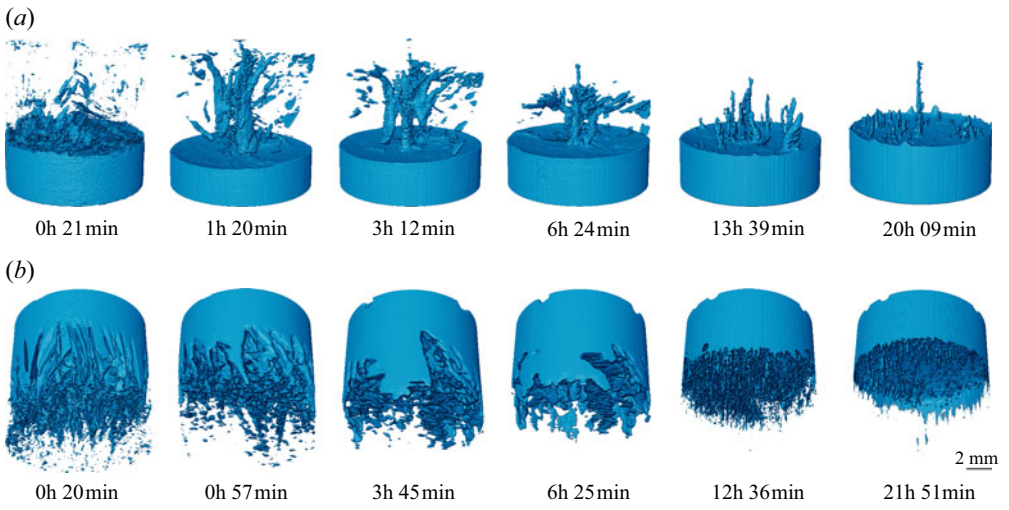


Figure 3. Microstructural evolution of brine structures. (*a*) Three-dimensional visualisation of large brine columns and their evolution during downward freezing. (*b*) Three-dimensional morphological evolution of brine skirts during upward freezing. More details of brine structural evolution are presented in figure S4.

continuously fall towards the warm end with time. Brine skirts (figure 3*b*, also see SI movie 3) around the central porous ice develop during upward freezing while brine columns are absent (see details in § S5). Note that the downward freezing also forms a reverse skirt in the end, shorter than that formed during upward freezing.

We infer that both the brine columns and skirts are induced by the coupling effect of gravity and the imperfect thermal boundary. As the side thermal insulation does not fully stop heat transfer from the environment to the specimen, the temperature around the periphery is always higher than that at the centre. During downward freezing, the salt concentration of brine coexisting with ice is higher in the centre according to the phase diagram, inducing a higher density. Gravity then favours the local downward brine flow. As the brine with higher concentration migrates to warmer areas, it melts the contacted ice and widens the flow path, which then facilitates additional flow. This positive feedback loop continues to form these thick brine columns. These brine columns likely resemble the brine channels seen in natural sea ice (Worster *et al.* 1997). We have also demonstrated that brine columns can develop within porous media (Jia *et al.* 2025), following a similar mechanism. More than one column can be formed. Therefore, we suggest that random localisation rather than the imperfect thermal boundary is dominant. The thickening of the brine columns feeds on the salt collected from adjacent areas. When brine in adjacent areas depletes or gets disconnected, the column thickening stops. During upward freezing, salt concentration and brine density are also higher in the centre, which can drive the saltier and denser brine flow towards the periphery. This transverse salt migration then impedes the ice growth at the periphery, which facilitates the formation of brine skirts.

3.4. *Pattern falling or rising*

Earlier formed striped patterns near the porous ice-brine interface, with regularly spaced brine and adjacent ice crystals, either fall in downward freezing or rise in upward freezing. These patterns form within the first hour after nucleation and gradually get pushed out of the porous ice within 4–6 h after nucleation. Migration towards the warm end can be quantified by tracking representative points A (see one example in figure 8(*d*) and more

https://doi.org/10.1017/jfm.2025.10633 Published online by Cambridge University Press

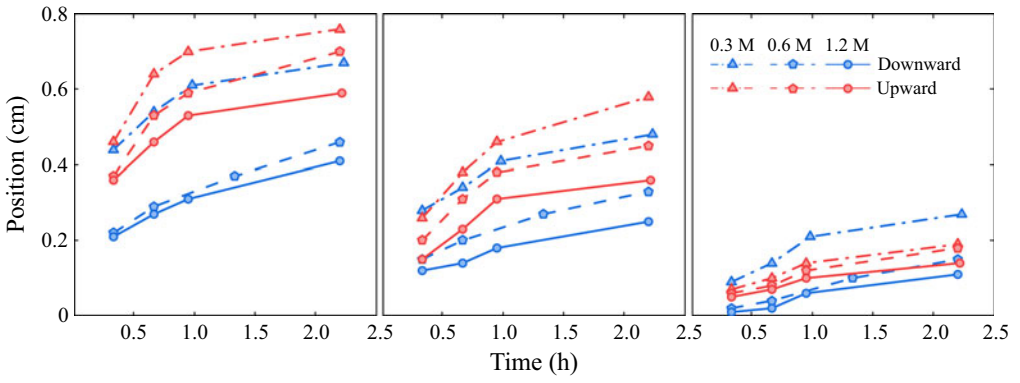


Figure 4. Movement of falling or rising brine stripes versus time obtained by tracking typical features.

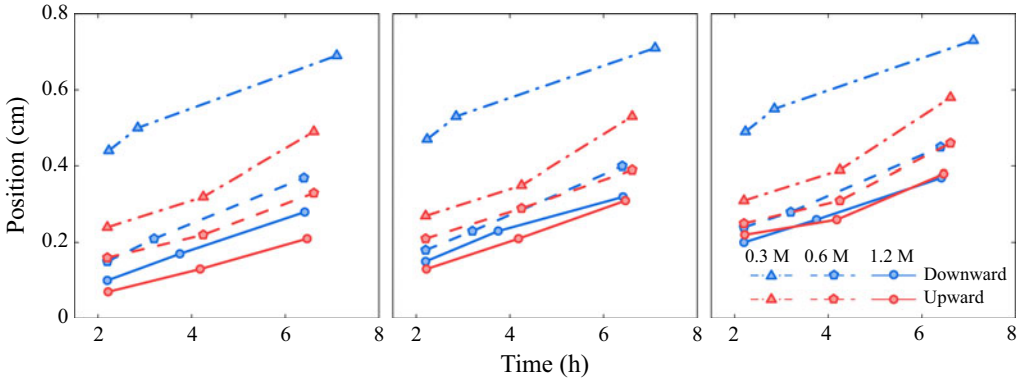


Figure 5. Movement of vertically aligned patterns versus time tracked by raw CT images.

examples in § S6, similarly, points B, C and D are selected to track other features). Figure 4 displays positions of points A versus time. The pattern migration velocity is higher with lower initial salt concentrations, regardless of downward or upward freezing. This velocity decreases with time. The difference between upward and downward freezing is not clear because the absolute position is dependent on point selection and the migration velocity demonstrates significant variations. Note that the falling or rising of patterns, involving extensive ice formation and melting, is complicated. These migrations include not only motion and stretching, but also merging and separation of brine pockets, and constant evolution of brine pocket outlines. Ions within one brine pocket are unlikely to stay within the original brine pocket.

3.5. *Vertical aligning*

Initially formed irregular patterns, with random inclinations, gradually transform into nearly vertical patterns. The final orientation of these patterns matches well with the thermal gradient (see details in § S7). We track the positions of points B at the interface between irregular and vertical patterns to investigate the alignment velocity (see details in § S6). Like the migration of points A, lower initial salt concentrations lead to faster transformation (figure 5). If we normalise the advancing velocity of points B by the case of 0.3 mol l^{-1} in either downward or upward freezing, the ratios among the three cases of 0.3, 0.6 and 1.2 mol l^{-1} are 1 : 0.89 : 0.80, showing little dependence on the influence of gravity.

https://doi.org/10.1017/jfm.2025.10633 Published online by Cambridge University Press

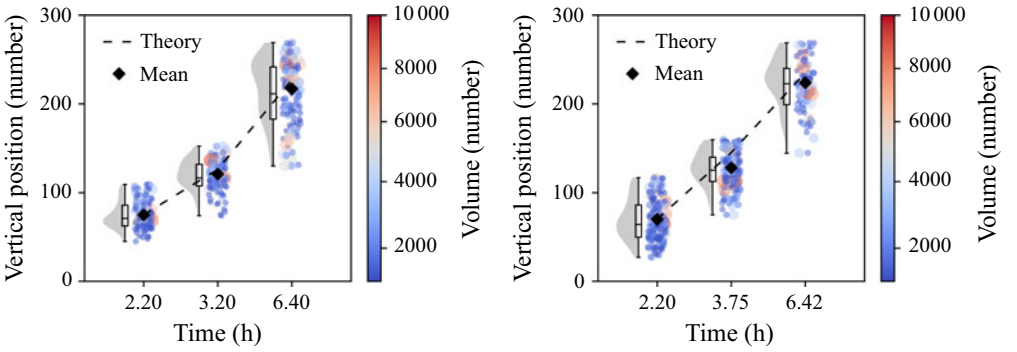


Figure 6. Vertical positions of brine pockets over time for both downward and upward freezings in 0.6 mol l^{-1} cases (the moment nucleation occurs is regarded as the origin). The scattered points represent individual brine pockets, while black diamonds indicate their mean positions.

3.6. *Brine pockets migration*

A great number of brine pockets within the aligned ice layer slowly migrate towards the freezing front. As individual brine pockets are difficult to identify, we filtered out just large brine pockets via image processing to track a group of smaller brine pockets (points C, see details in § S6). Since these brine pockets are nearly parallel to the temperature gradient, we infer that ion diffusion driven by the brine concentration gradient $\mathrm{d}c/\mathrm{d}z$, induced by the temperature gradient $\mathrm{d}T/\mathrm{d}z$ and phase boundary $\mathrm{d}c/\mathrm{d}T$, is the dominant mechanism. As ions diffuse towards the warm end, ice forms at the cold end of the brine pocket and melts at the warm end. According to Fick's law and mass conservation, this mechanism is described by a migration rate of (Harrison 1965; Hoekstra *et al.* 1965)

$$|v| = -\frac{D}{c}\frac{\mathrm{d}c}{\mathrm{d}T}\frac{\mathrm{d}T}{\mathrm{d}z}, \tag{3.1}$$

where the v is the velocity of brine pockets, c is the local salt concentration and D is the mass diffusion coefficient. Figure 6 demonstrates both the experimental results (black diamonds) and theoretical calculations (dashed line). The good match, regardless of freezing direction, suggests that temperature gradient-induced diffusion rather than gravity is the dominant factor.

3.7. *Cleaner ice layer thickening*

A layer of cleaner ice becomes obvious at around 3 h after the nucleation. Note that ice in this layer is not 100 % pure, but contains minute brine pockets, as discussed in the previous section. This layer thickens with time as the trapped brine stripes move towards the warm end. We assess the velocities of thickening by manually tracking positions of representative points D at the boundary of the cleaner ice layer in the raw tomograms (see details in § S6). Figure 7(*a*) shows the positions of these points versus time under various conditions, and the relation between them looks linear. In three downward freezing cases, a lower initial salt concentration produces a thicker layer and higher thickening rate. If we consider salt diffusion in the adjacent striped brine as the governing mechanism, i.e. the transfer of salt in the porous ice determines the thickening rate, the thickening rate should be only dependent on the local salt concentration at points D and the temperature gradient, as seen in (3.1). The initial thought is that initial salt concentration should be irrelevant. However, the initial salt concentration affects the boundary between porous ice and brine,

https://doi.org/10.1017/jfm.2025.10633 Published online by Cambridge University Press

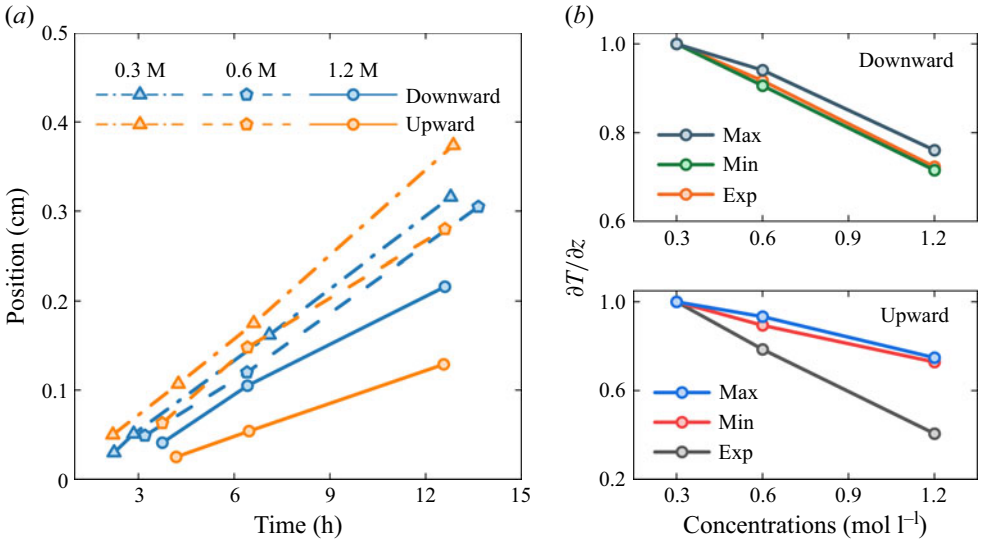


Figure 7. (*a*) Thickening of cleaner ice layers as a function of time. (*b*) Initial concentration effects on dimensionless temperature gradients $\partial T/\partial z$. The initial concentration varies from 0.3, 0.6 to 1.2 mol l^{-1}.

which then affects the local temperature gradient. The temperature gradient in low initial salt concentration cases is higher in the porous ice due to a larger portion of porous ice in the whole specimen (see the calculation in § S8). The ratio among thickening rates for three initial salt concentrations match well with the ratio among the corresponding temperature gradients (figure 7*b*). We therefore suggest that diffusion of adjacent striped brine is the dominant factor for cleaner ice layer thickening.

Similar trends can be found in upward freezing cases, i.e. thicker layers and higher thickening rates correlate with lower initial salt concentrations. However, the ratio among thickening rates does not match with the ratio among temperature gradients (figure 7*b*). If we look at the original CT images (figure 1*b*), the formation of a cleaner ice layer is obviously more difficult in upward freezing, especially with higher initial salt concentrations. Some brine stripes persist in the porous ice until the end of experiments in the 0.6 and 1.2 mol l^{-1} cases. Ideally, upward salt diffusion driven by the concentration gradient should not be influenced by gravity. However, gravity seems to play an important role in wider brine stripes and hinders the upward salt migration. Although at a smaller scale, gravity-driven salt migration towards lower elevations, similar to the formation mechanism of a brine skirt, can potentially explain this trend.

Note that residual brine pockets persist throughout the freezing process within the relatively clean ice layer. Although the overall volume fraction of trapped brine is lower near the cold end and gradually decreases with time, there are tiny brine pockets (mostly thinner than 35 μm) even at the cold end by the end of the experiments. This behaviour cannot be explained by ion diffusion. If the governing equations based on diffusion are universally applicable to all brine pockets, complete expulsion from the porous ice matrix would be expected over time. Therefore, we suggest that there is a mechanism to trap some brine pockets or at least slow down the diffusion and impede the formation of a pure ice layer. Higher free energy level at the boundaries between single crystals can also potentially play a role.

https://doi.org/10.1017/jfm.2025.10633 Published online by Cambridge University Press

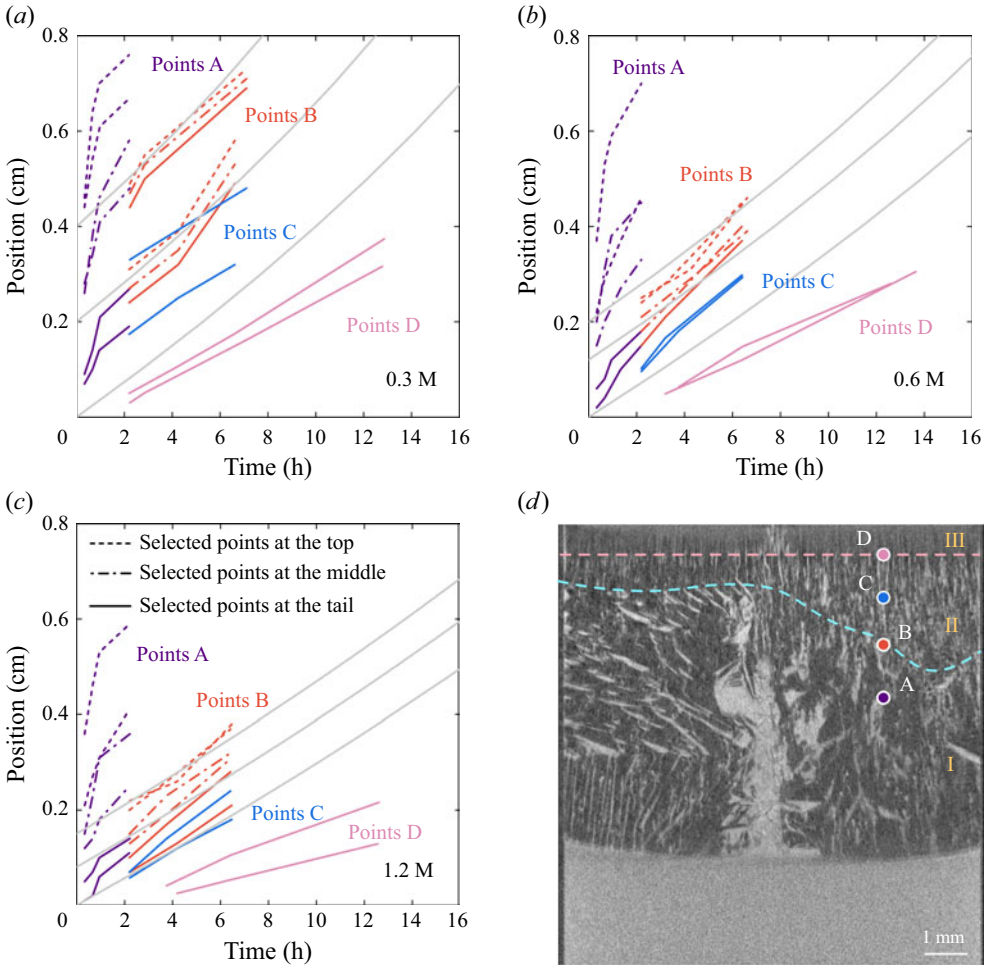


Figure 8. Evolution of representative points within typical groups during freezing. Panels (*a*), (*b*) and (*c*) display cases with 0.3, 0.6 and 1.2 M of initial salt concentration. (*d*) Separation of different zones and examples of representative points A pattern falling or rising, points B vertical alignment, points C brine pockets migration and points D cleaner ice layer. Multiple points have been selected for points A and B, therefore there are several lines. We use dotted lines to denote the position of points at the front, broken for that in the middle and solid for that at the tail. Grey lines represent the predicted position of pockets following ideal diffusion.

3.8. *Comparison of migration rates*

The vertical sections of the specimens can be separated into three zones, as shown in figure 8(*d*). Zone I features fast falling or rising inclined brine stripes (purple lines). The border between zones I and II is the shift from random inclined stripes to aligned vertical stripes, which are not perfectly horizontal but zigzagged (blue broken lines). Brine stripes in zone II fall slower than in zone I (red lines). Behind the tale of falling brines in zone II, a relative but not 100 % pure ice layer is leftover and classified as zone III. The boundary between zones II and III is smooth (pink broken lines). Brine columns mainly occur in zone I.

The overall migration rate follows the order of (A) brine stripe falling in zone I $\approx$ brine column sinking $>$ (B) vertical aligning $>$ (C) brine stripe falling in zone II $>$ (D) cleaner ice layer thickening. The grey solid lines are the predicted migration of ideal

https://doi.org/10.1017/jfm.2025.10633 Published online by Cambridge University Press

brine pockets, initiated at different vertical positions, driven solely by diffusion (see the derivation in § S9). Red and blue lines, which represent ice crystals aligning and brine pocket migration in vertical porous ice, are roughly parallel to the theoretical derivations, indicating diffusion-dominant processes. The migration rate of brine stripes in zone I (slope angle of purple lines) is obviously faster in the first hour after nucleation but gradually converges to the prediction by diffusion in the following hour. This reduction in migration rate occurs in both downward and upward freezings, which indicates that gravity does not contribute. We suspect it to be related to heat transfer coupled with phase transformation because the duration of roughly one hour agrees well with the time required for the system to reach thermal equilibrium (corresponding to state S3).

Note that the tale of thicker brine columns does not advance faster than the thinner brine stripes, which indicates that the contribution of convection in the larger channels is not distinguishable from the convection in the smaller channels, even when convection plays a role. The expansion rate of the cleaner ice layer (zone III), as displayed by the pink lines, is slower than the prediction by solely diffusion. This means that there is a limiting factor that impedes diffusion in the porous ice, which could be associated with the complex brine network geometry and potentially interfacial interactions such as adsorption. This slower migration than diffusion is also a new mechanism, which requires further theoretical and experimental investigation.

3.9. *Concentration of trapped salt in the porous ice*

The average salt concentration in the porous ice is a critical parameter for seawater desalination and geophysical studies on sea ice. We calculated the salt mass according to the brine volume and local concentration as determined from the phase boundary and local temperature. The vertical salt concentration profile and its evolution during either downward or upward freezing for the 0.6 mol l^{-1} cases are plotted in figures 9(*a*) and 9(*b*), with the cold end at $Z = 0$ mm and $Z = 10$ mm, respectively. As the trapped brine migrates towards the warmer end, the salt concentration in the porous ice gradually decreases. If we consider only one-dimensional diffusion, the salt concentration profile should follow a vertical translational motion and mild stretching. However, the salt concentration at each point decreases with time, which proves the brine pockets' horizontal thinning in addition to the vertical motion. This indicates there is a driving mechanism for ice to grow horizontally to push the brine pockets out. Furthermore, the violation of mass conservation in seemingly individual brine pockets, as identified in CT images, also implies smaller paths in the ice to transport the excluded ions. The size of these paths exceeds the resolution of CT scanning in this study. It therefore could be at the nanoscale. We speculate the brine veins among adjacent single crystals (Vetráková *et al.* 2019) serve as these paths.

The overall desalination efficiency, defined as the mass of salt rejected from the porous ice to the liquid reservoir divided by the initial mass of salt, increases with time (figure 9*c*). Downward freezing (blue lines) achieves higher desalination efficiency than upward freezing, highlighting the facilitation of gravity. Interestingly, the desalination efficiency in the high molarity brine case is higher during downward freezing, while the trend is the opposite during upward freezing. In all cases except for the upward freezing of the 1.2 mol l^{-1} case, the desalination efficiency exceeds 90 % after 22 h, producing 5–7 mm thick cleaner ice.

4. Implication for natural and industrial processes

Ice structures and brine patterns reported in this study, as well as the isolated governing physics, can help enhance our understanding of seawater freezing and directional

https://doi.org/10.1017/jfm.2025.10633 Published online by Cambridge University Press

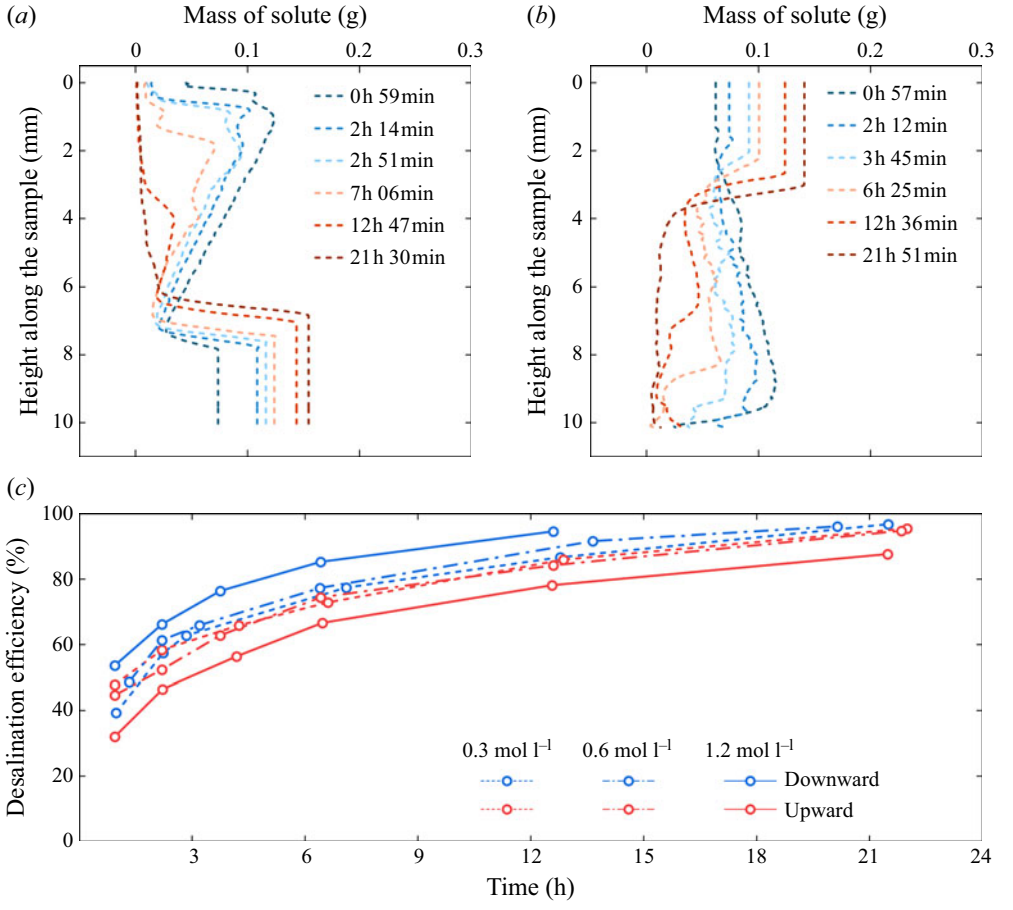


Figure 9. (*a*), (*b*) Mass profiles of solute for each slice along the vertical height. (*c*) Desalination efficiency as a function of time at different initial salt concentrations.

solidification in other solution systems. Note that directional solidification is universal in the three-dimensional world as cooling must start from the surface towards the material centre, making local solidification always directional. For example, downward freezing in high salinity solutions can be more efficient in freezing desalination (Gu *et al.* 2012). From a geophysical perspective, the structure and evolution of sea ice can follow a similar pattern as described in this study. Polygonal ice patterns (Knight 1962), brine channels and veins (Worster *et al.* 1997) and trapped brine pockets (de Angelis *et al.* 2005) have been reported before, and we show here how they emerge and evolve with time. The principles of directional solidification extend to freeze casting, single crystal growth and superalloy manufacturing (Fu & Geng 2001; Deville 2013; Fortuna *et al.* 2021). In frozen food processing, ice recrystallisation and solute migration affect texture and quality (Sun *et al.* 2023). The porous ice structures observed in this study resemble the microstructure of frozen tissues and biomaterials, which is crucial for cryogenic preservation of biological samples (Qin *et al.* 2020).

A KI solution instead of NaCl seawater is used in this study to achieve better image resolution. Actual seawater freezing can deviate due to differences in (i) the salt-water phase diagram, (ii) the brine density at the same molarity and (iii) ionic properties such as hydration radii and interfacial repulsion. These factors can affect the phase equilibrium,

https://doi.org/10.1017/jfm.2025.10633 Published online by Cambridge University Press

convection and molecular level ion exclusion. However, the governing physical processes such as heat conduction and ion diffusion are similar. Overall, the direct applicability of the results and conclusions of this study to natural seawater freezing is promising. For example, the thickening rate of the cleaner ice layer can help to optimise the time duration for brine exclusion before ice harvesting, and the freezing of high salt concentration solutions can also be made efficient in desalination.

5. Conclusions

This study investigates microscopic details of the brine freezing dynamics during directional solidification by *in situ* X-ray CT scanning. Quantitative tracking of brine features through three-dimensional image processing demonstrates the brine migration and ice structure transformation. The extracted data and theoretical analyses provide unprecedented insight into the freezing kinetics.

Brine freezing can be roughly divided into three stages. The first stage, typically lasting for several seconds, starts from nucleation to local equilibrium, considered independent of both long-range heat and mass transfer. The second stage ends when the system reaches a roughly global thermal equilibrium. Long-range mass transfer, which follows, involves brine expulsion induced by volume expansion, and especially for downward freezing, convection as a rapid brine exclusion mechanism. The third stage is featured by the slow mass transfer dominated by diffusion, along with a new and even slower mechanism. There is still residual brine trapped in the porous ice at the end because diffusion does not fully purify the porous ice.

Morphologically, relatively random striped patterns form initially in the first and second stages. The evolution of ice structure and brine pattern is dynamic in the third stage. Brine columns in downward freezing and brine skirts in upward freezing emerge in the striped patterns. These striped patterns are later replaced by vertically aligned and horizontally polygonal patterns. Brine pockets trapped in the porous ice gradually migrate through nanoscale paths to the warm end and are reduced in volume. In the end, both downward and upward freezings reach a similar state with just porous ice and residual polygonal brine veins.

These findings and visualisation offer new perspectives for understanding natural sea ice formation, freeze desalination, cryogenic preservation and many other similar situations.

Supplementary material and movies. Supplementary material and movies are available at https://doi.org/10.1017/jfm.2025.10633.

Funding. This work is supported by National Natural Science Foundation of China (Grant No. 42472353) and by Key Development Program of Zhejiang Province (Grant No. 2023SDXHDX0005).

Declaration of interests. The authors report no conflict of interest.

References

ANDERSON, D.M., GUBA, P. & WELLS, A.J. 2022 Mushy-layer convection. *Phys. Today* **75**, 34–39.

AUSSILLOUS, P., SEDERMAN, A.J., GLADDEN, L.F., HUPPERT, H.E. & WORSTER, M.G. 2006 Magnetic resonance imaging of structure and convection in solidifying mushy layers. *J. Fluid Mech.* **552**, 99–125.

KNIGHT, C.A. 1962 Polygonization of aged sea ice. *J. Geology* **70**, 240–246.

CHAYEN, N.E. & SARIDAKIS, E. 2008 Protein crystallization: from purified protein to diffraction-quality crystal. *Natl Methods* **5**, 147–153.

CHEN, X. *et al.* 2022 Snow flea antifreeze peptide for cryopreservation of lactic acid bacteria. *npj Sci. Food* **6**, 10.

CHU, F. *et al.* 2024 Interfacial ice sprouting during salty water droplet freezing. *Natl Commun.* **15**, 2249.

https://doi.org/10.1017/jfm.2025.10633 Published online by Cambridge University Press

DANIELS, K.E., PLAPP, B.B. & BODENSCHATZ, E. 2000 Pattern formation in inclined layer convection. *Phys. Rev. Lett.* **84**, 5320–5323.

DE ANGELIS, M., MOREL-FOURCADE, M., BARNOLA, J., SUSINI, J. & DUVAL, P. 2005 Brine micro-droplets and solid inclusions in accreted ice from Lake Vostok (East Antarctica). *Geophys. Res. Lett.* **32**, 2005GL022460.

DEVILLE, S. 2013 Ice-templating, freeze casting: beyond materials processing. *J. Mater. Res.* **28**, 2202–2219.

DU, Y., CALZAVARINI, E. & SUN, C. 2024 The physics of freezing and melting in the presence of flows. *Natl Rev. Phys.* **6**, 676–690.

DU, Y., WANG, Z., JIANG, L., CALZAVARINI, E. & SUN, C. 2023 Sea water freezing modes in a natural convection system. *J. Fluid Mech.* **960**, A35.

FELTHAM, D.L., UNTERSTEINER, N., WETTLAUFER, J.S. & WORSTER, M.G. 2006 Sea ice is a mushy layer. *Geophys. Res. Lett.* **33**.

FORTUNA, S.V. & *et al.* 2021 Directional solidification of a nickel-based superalloy product structure fabricated on stainless steel substrate by electron beam additive manufacturing. *Metall Mater Trans A* **52**, 857–870.

FU, H. & GENG, X. 2001 High rate directional solidification and its application in single crystal superalloys. *Sci. Technol. Adv. Mat.* **2**, 197–204.

GALLEY, R.J., & *et al.* 2015 Imaged brine inclusions in young sea ice – Shape, distribution and formation timing. *Cold Reg. Sci. Technol.* **111**, 39–48.

GU, W. *et al.* 2012 Sea ice desalination under the force of gravity in low temperature environments. *Desalination* **295**, 11–15.

HARRISON, J.D. 1965 Measurement of brine droplet migration in ice. *J. Appl. Phys.* **36**, 3811–3815.

HOEKSTRA, P., OSTERKAMP, T.E. & WEEKS, W.F. 1965 The migration of liquid inclusions in single ice crystals. *J. Geophys. Res.* **70**, 5035–5041.

JIA, J., GAO, X., WU, Z. & LEI, L. 2025 4D freeze-driven purification of heavy-metal contaminated sandy soil. *J. Clean. Prod.* **489**, 144676.

KAMM, P.H. *et al.* 2023 X-ray tomoscopy reveals the dynamics of ice templating. *Adv. Functional Mater. n/a* **2304738**.

KATZ, R.F. & WORSTER, M.G. 2008 Simulation of directional solidification, thermochemical convection, and chimney formation in a Hele-Shaw cell. *J. Comput. Phys.* **227**, 9823–9840.

LEI, L., SEOL, Y. & JARVIS, K. 2018 Pore-scale visualization of methane hydrate-bearing sediments with micro-CT. *Geophys. Res. Lett.* **45**, 5417–5426.

MALLEY, P.P.A., CHAKRABORTY, S. & KAHAN, T.F. 2018 Physical characterization of frozen saltwater solutions using raman microscopy. *ACS Earth Space Chem.* **2**, 702–710.

MARCELLINI, M., NOIRJEAN, C., DEDOVETS, D., MARIA, J. & DEVILLE, S. 2016 Time-lapse, *in situ* imaging of ice crystal growth using confocal microscopy. *ACS Omega* **1**, 1019–1026.

MAUS, S., BAHAFID, S., HENDRIKS, M., JACOBSEN, S. & GEIKER, M.R. 2023 X-ray micro-tomographic imaging and modelling of saline ice properties in concrete frost salt scaling experiments. *Cold Reg. Sci. Technol.* **208**, 103780.

MAUS, S., SCHNEEBELI, M. & WIEGMANN, A. 2021 An x-ray micro-tomographic study of the pore space, permeability and percolation threshold of young sea ice. *The Cryosphere* **15**, 4047–4072.

MIDDLETON, C.A., THOMAS, C., DE WIT, A. & TISON, J.-L.2016 Visualizing brine channel development and convective processes during artificial sea-ice growth using Schlieren optical methods. *J. Glaciol.* **62**, 1–17.

NIELD, D.A. 1994 Convection induced by an inclined temperature gradient in a shallow horizontal layer. *Int. J. Heat Fluid Fl.* **15**, 157–162.

NOTZ, D. & WORSTER, M.G. 2009 Desalination processes of sea ice revisited. *J. Geophys. Res.* **114**, 2008JC004885.

OGGIER, M. & EICKEN, H. 2022 Seasonal evolution of granular and columnar sea ice pore microstructure and pore network connectivity. *J. Glaciol.* **1–16** https://doi.org/10.1017/jog.2022.1.

ORTIZ-PÉREZ, A.S. & DÁVALOS-OROZCO, L.A. 2011 Convection in a horizontal fluid layer under an inclined temperature gradient. *Phys. Fluids* **23**, 084107.

QIN, K., *et al.* 2020 Unveiling cells' local environment during cryopreservation by correlative, *in situ*, spatial and thermal analyses. *J. Phys. Chem. Lett.* **11**, 7730–7738.

RAPHAEL, M.N., MAIERHOFER, T.J., FOGT, R.L., HOBBS, W.R. & HANDCOCK, M.S. 2025 A twenty-first century structural change in Antarctica's sea ice system. *Commun. Earth Environ.* **6**, 1–9.

SHISHKINA, O. 2021 Rayleigh-Bénard convection: the container shape matters. *Phys. Rev. Fluids* **6**, 090502.

SUN, L. *et al.* 2023 Regulating ice formation for enhancing frozen food quality: materials, mechanisms and challenges. *Trends Food Sci. Tech.* **139**, 104116.

https://doi.org/10.1017/jfm.2025.10633 Published online by Cambridge University Press

TESTÓN-MARTÍNEZ, S. *et al.* 2024 Experimental modelling of the growth of tubular ice brinicles from brine flows under sea ice. *The Cryosphere* **18**, 2195–2205.

TSIRONI, I. *et al.* 2020 Brine rejection and hydrate formation upon freezing of NaCl aqueous solutions. *Phys. Chem. Chem. Phys.* **22**, 7625–7632.

VETRÁKOVÁ, Ľ., NEDĚLA, V., RUNŠTUK, J. & HEGER, D. 2019 The morphology of ice and liquid brine in an environmental scanning electron microscope: a study of the freezing methods. *The Cryosphere* **13**, 2385–2405.

VRBKA, L. & JUNGWIRTH, P. 2005 Brine rejection from freezing salt solutions: a molecular dynamics study. *Phys. Rev. Lett.* **95**, 148501.

WANG, R. *et al.* 2023 Unsynchronized migrations of different salt ions and ice microstructure development during unidirectional freeze–thaw. *Desalination* **549**, 116326.

WANSCHURA, M., KUHLMANN, H.C. & RATH, H.J. 1996 Three-dimensional instability of axisymmetric buoyant convection in cylinders heated from below. *J. Fluid Mech.* **326**, 399–415.

WELLS, A.J., HITCHEN, J.R. & PARKINSON, J.R.G. 2019 Mushy-layer growth and convection, with application to sea ice, *Phil. Trans. R. Soc. A.* **377** 20180165.

WETTLAUFER, J.S., WORSTER, M.G. & HUPPERT, H.E. 1997 Natural convection during solidification of an alloy from above with application to the evolution of sea ice. *J. Fluid Mech.* **344**, 291–316.

WHITMAN, W.G. 1926 Elimination of salt from sea-water ice. *Am. J. Sci.* **s5-11**, 126–132.

WILLIAMS, P.M. *et al.* 2015 Technology for freeze concentration in the desalination industry. *Desalination* **356**, 314–327.

WORSTER, M.G. 1990 Structure of a convecting mushy layer. *Appl. Mech. Rev.* **43**, S59–S62.

WORSTER, M.G. & REES JONES, D.W. 2015 Sea-ice thermodynamics and brine drainage, *Phil. Trans. R. Soc. A.* **373** 20140166.

WORSTER, M.G. & WETTLAUFER, J.S. 1997 Natural convection, solute trapping, and channel formation during solidification of saltwater. *J. Phys. Chem. B* **101**, 6132–6136.

YANG, H. *et al.* 2025 Study on freezing separation process through observing microstructure of NaCl solution ice. *Sep. Purif. Technol.* **355**, 129674.

ZHANG, T., WANG, Z., WANG, L., LI, J. & WANG, J. 2022 In-situ comparison of interface instability of basal and edge planes during unidirectional growth of sea ice. *J. Colloid Interf. Sci.* **625**, 169–177.

ZHAO, C., LIN, Y., WU, X., ZHANG, X. & CHU, F. 2023 Nanoscale insights on the freezing front propagation and ion behaviors during seawater freezing. *Appl. Surf. Sci.* **641**, 158499.

https://doi.org/10.1017/jfm.2025.10633 Published online by Cambridge University Press